



Provided by the author(s) and University of Galway in accordance with publisher policies. Please cite the published version when available.

Title	Experimental characterisation and computational modelling for cyclic elastic-plastic constitutive behaviour and fatigue damage of X100Q for steel catenary risers
Author(s)	Devaney, Ronan J.; O'Donoghue, Padraic E.; Leen, Sean B.
Publication Date	2018-06-21
Publication Information	Devaney, Ronan J., O'Donoghue, Padraic E., & Leen, Sean B. (2018). Experimental characterisation and computational modelling for cyclic elastic-plastic constitutive behaviour and fatigue damage of X100Q for steel catenary risers. <i>International Journal of Fatigue</i> , 116, 366-378. doi: <a href="https://doi.org/10.1016/j.ijfatigue.2018.06.032">https://doi.org/10.1016/j.ijfatigue.2018.06.032</a>
Publisher	Elsevier
Link to publisher's version	<a href="https://doi.org/10.1016/j.ijfatigue.2018.06.032">https://doi.org/10.1016/j.ijfatigue.2018.06.032</a>
Item record	<a href="http://hdl.handle.net/10379/15587">http://hdl.handle.net/10379/15587</a>
DOI	<a href="http://dx.doi.org/10.1016/j.ijfatigue.2018.06.032">http://dx.doi.org/10.1016/j.ijfatigue.2018.06.032</a>

Downloaded 2024-04-25T04:37:51Z

Some rights reserved. For more information, please see the item record link above.



# EXPERIMENTAL CHARACTERISATION AND COMPUTATIONAL MODELLING FOR CYCLIC ELASTIC- PLASTIC CONSTITUTIVE BEHAVIOUR AND FATIGUE DAMAGE OF X100Q FOR STEEL CATENARY RISERS

Ronan J. Devaney<sup>1,3</sup>, Padraic E. O'Donoghue<sup>2,3</sup>, Sean B. Leen<sup>\*1,3</sup>

<sup>1</sup>*Mechanical Engineering, College of Engineering & Informatics, NUI Galway, Ireland.*

<sup>2</sup>*Civil Engineering, College of Engineering & Informatics, NUI Galway, Ireland.*

<sup>3</sup>*Ryan Institute for Environmental, Marine and Energy Research, NUI Galway, Ireland.*

[\\*sean.leen@nuigalway.ie](mailto:sean.leen@nuigalway.ie) – +35391 495 955

**Abstract:** New higher strength steels are required for deep and ultra-deepwater steel catenary risers (SCRs). In this work, the cyclic elastic-plastic-damage behaviour of X100Q, a candidate next-generation SCR material is experimentally characterised and modelled. The material is shown to exhibit early life (primary) fatigue damage followed by the more conventional (secondary) fatigue damage; as a result, it is necessary to demarcate the observed cyclic softening into dynamic recovery and damage-induced softening. An automated constitutive parameter optimisation process in combination with a new two-stage cyclic damage evolution model successfully predicts the effect of strain-range on damage evolution. The model is implemented in a user material (UMAT) subroutine for multiaxial application, within a hierarchical global-local modelling methodology for dynamic fatigue analysis of an SCR girth weld geometry. The interdependency between fatigue damage-induced material degradation and cyclic plasticity at the weld is shown for a range of load cases.

**Keywords:** Damage mechanics; Fatigue; Offshore; Welded joints

## 1. Introduction

High-strength low-alloy (HSLA) steels are an important category of engineering materials, which are used across a variety of domains, from the automotive and shipbuilding industries to applications such as pipelines and cranes. Some of the key

advantages which have contributed to the development of HSLA steels are:

- The cost savings attainable when compared with using alternative high-strength materials.
- The high weldability of the material due to the low level of carbon and alloying elements.
- The design and fabrication benefits which are attainable from using higher strength steels and thus producing lighter structures.
- The commercial development of new production methods such as thermomechanically controlled processing and accelerated cooling [1], which have allowed for fine-grained steels with high strength and toughness to be produced.

Due to the cyclic loading experienced in many applications of HSLA steels, it is important to characterise the material behaviour under both monotonic and fatigue loading. SCRs are an application of HSLA steels where both monotonic strength and fatigue resistance are critical. SCRs are pipelines used to transfer oil, gas and injection fluids between subsea wellheads and production facilities, as shown in Figure 1. The dynamic loading experienced by SCRs as a result of vessel motion, vortex-induced vibrations and seabed phenomena such as pipeline walking [2] make fatigue a primary challenge for the design and installation of SCRs. Due to the highly unpredictable loading environment, it is standard practice to specify SCR components with conservative factors of safety between 7 and 10 [3].

In particular, stress concentrations such as welded connections have long been recognised as a primary source of fatigue failure in the offshore oil and gas industry. A recent computational study by the authors [4] on SCR girth welds found elastic stress concentration factors of between 1.6 and 4.5 at the weld due to the combined effect of the

geometrical discontinuity and material mismatch, indicating that the weld is a critical location in terms of fatigue performance.

There is significant work in the literature on fatigue analysis. The early work is focused on total life approaches, which extrapolate from S-N curves for fatigue life estimation, such as the well-known relations developed by Basquin, Coffin and Manson [5], [6], [7]. While such approaches are useful for initial design purposes, they do not capture the fatigue damage-induced degradation of material properties through the life of a component. More recently, damage mechanics methodologies have been applied to model fatigue, which use a continuum approach to model the initiation and coalescence of microscopic internal defects to form a macro-scale crack, after which rapid propagation occurs and a fracture mechanics approach may be adopted. Chaboche developed the uniaxial non-linear continuous damage (NLCD) high-cycle fatigue (HCF) model [8], which was then adopted into the damage coupled constitutive relationship and extended to the multiaxial case by Chaudonneret [9]. This model has been implemented in simulations of fatigue in notched Ti-6Al-4V specimens by Marmi et al. [10] and Zhang et al. [11]. Marmi applied the model in the integrated form as a post-processor to finite element (FE) analyses, while Zhang used a local incremental implementation, through an Abaqus UMAT subroutine. The local incremental application of the model was shown to predict fatigue lives closest to the experimental lives when compared with the local or non-local integrated models for each load case.

However, a limitation of this model is its inability to account for damage-induced plasticity or plastic strain based damage. This is particularly important for the common scenario of a nominally elastic applied stress, with features such as welds or defects causing localised stresses exceeding yield with plastic deformation occurring. Shen and co-workers [12] recently implemented an elastic-plastic nonlinear kinematic hardening

(NLKH) model coupled with the NLCD HCF and Lemaitre strain energy density (SED) low-cycle fatigue (LCF) models [13], within an Abaqus UMAT subroutine. In their work, a programme of FE simulations was conducted for tension-compression loading on a notched bar and bending-torsion loading on a Society of Automotive Engineers notched shaft. The predictions for the notched bar were within a factor of 0.4 of the experimental lives and a factor of 6.1 for the SAE notched shaft case. However, cyclic hardening-softening and the experimental damage evolution were not considered during parameter identification. Therefore the predicted damage evolution, although nonlinear, was not shown to be representative of the material degradation.

Both the NLCD and SED models predict damage evolution, but neither model is capable of capturing the two-stage LCF damage evolution which may be exhibited in quenched and tempered (Q&T) HSLA steels as shown in Figure 2. Thus they neglect the damage-induced material degradation which is present for the majority of component life. In the present work a new two-stage LCF damage model based on effective accumulated plastic strain is proposed to account for early life damage, and the resultant degradation in material properties. To address the challenge of demarcating cyclic softening as a result of early-stage microcracking damage [13] from softening as a result of microstructural evolution ([14], [15], [16]), a new parameter optimisation procedure is proposed, which takes account of the experimentally measured damage. The optimisation procedure is implemented within a uniaxial cyclic plasticity MATLAB code, encompassing the Levenberg-Marquardt algorithm.

The two-stage fatigue damage model proposed here is calibrated and validated through a programme of LCF tests conducted on the bainitic HSLA steel X100Q. The two-stage damage model is then implemented in combination with an elastic-plastic nonlinear kinematic and isotropic hardening (NLKIH) plasticity model and the NLCD HCF model,

within a 3D Abaqus UMAT subroutine. The fatigue damage UMAT is applied in combination with a global-local modelling methodology for the analysis of SCR girth welds, with dynamic multiaxial loading obtained from the offshore structural analysis FE package Flexcom [17]. The fatigue lives predicted are compared with the critical-plane Smith Watson Topper method [18], and the damage accumulation and material degradation at the weld as a result of geometrical discontinuity are examined.

## **2. Experimental methodology**

### **2.1. Material**

X100Q is a fine-grained Q&T HSLA steel, with chemical composition and mechanical properties in accordance with the oil and gas industry standard for line pipe API 5L [19]. The high strength requirements are achieved through the addition of grain refining aluminium and precipitation strengthening by microalloying with niobium and titanium. The chemical composition reported by the plate manufacturer is shown in Table 1. The plate was heat treated by holding at 920°C for 7 minutes before being quenched with water, followed by tempering at 600°C for 1 minute and then air cooled. The as-received material is in the form of two 406.4 mm outer diameter, 25 mm wall thickness, 2 m long seam welded pipe sections.

### **2.2. Testing procedure**

Specimens for microstructural analysis were manufactured from the as-received material, mounted in epoxy resin, then ground and polished to a 0.06 µm finish using a diamond suspension and etched using Vilella's reagent. Microscopy was performed using an Olympus BX51M optical microscope and a Hitachi S-4700 SEM at NUI Galway.

Tensile and LCF specimens were prepared in accordance with the ASTM E8 [20]

and ASTM E606 [21] standards respectively. The LCF specimens were machined to a gauge length and diameter of 16 mm and  $\varnothing 6.5$  mm respectively, then polished to an average surface roughness of 0.2  $\mu\text{m}$  on the gauge length. LCF tests were conducted at room temperature on a 100 kN Instron 8500 closed loop servohydraulic system, with hydraulic grips and V-shaped jaws, using strain controlled fully reversed loading. Testing was conducted at four strain ranges from 0.6% to 1% using a sinusoidal waveform at a strain rate of 0.2%/s. Strain was measured via a knife-edge extensometer which was fixed to the gauge length by elastic bands.

### 3. Computational modelling

#### 3.1. Damage coupled constitutive model

Under the damage mechanics theory first described by Kachanov [22] and Rabotnov [23], damage is modelled as an effective reduction in load resisting area. A schematic diagram illustrating the definition of damage normal to the direction  $\vec{n}$  is shown in Figure 3, where  $S_D$  is the total area of defects and  $S$  is the area of a material element identified by its normal  $\vec{n}$ . If the assumption of isotropic damage is used, the effective load resisting area  $\tilde{S}$  may be represented as follows:

$$\tilde{S} = S - S_D = S(1 - D) \quad (1)$$

therefore, by definition, the effective stress  $\tilde{\sigma}$  is given by:

$$\tilde{\sigma} = \frac{\sigma S}{\tilde{S}} = \frac{\sigma}{(1 - D)} = E \varepsilon^e \quad (2)$$

The Chaboche NLKIH plasticity model [24] is used for constitutive modelling in this study. The model is modified to incorporate damage through the use of an effective stress term in the elasticity law on the basis of strain equivalence, as follows:

$$\varepsilon^e = \frac{1 + \nu}{E} \left( \frac{\boldsymbol{\sigma}}{1 - D} \right) - \frac{\nu}{E} \left( \frac{\text{Tr}(\boldsymbol{\sigma})}{1 - D} \right) \quad (3)$$

where  $\boldsymbol{\varepsilon}^e$  is the elastic strain tensor,  $\boldsymbol{\sigma}$  is the stress tensor,  $E$  and  $\nu$  are the elastic modulus and Poisson's ratio of the undamaged material. The multiaxial yield function with damage is shown as follows:

$$f = \left( \frac{\boldsymbol{\sigma}}{1-D} - \boldsymbol{\chi} \right)_{\text{eq}} - R - k \quad (4)$$

where  $\boldsymbol{\chi}$  is the kinematic back-stress tensor,  $R$  is the isotropic change in the yield surface due to cyclic softening,  $k$  is the cyclic yield stress and eq denotes von Mises stress. The increment in plastic strain is calculated as follows:

$$\dot{\boldsymbol{\varepsilon}}^p = \dot{\lambda} \frac{df}{d\boldsymbol{\sigma}} = \frac{3}{2} \frac{\dot{\lambda}}{1-D} \frac{\left( \frac{\boldsymbol{\sigma}}{1-D} - \boldsymbol{\chi} \right)_{\text{dev}}}{\left( \frac{\boldsymbol{\sigma}}{1-D} - \boldsymbol{\chi} \right)_{\text{eq}}} \quad (5)$$

where  $\dot{\boldsymbol{\varepsilon}}^p$  is the increment in plastic strain tensor,  $\dot{\lambda}$  is the plastic multiplier, dev denotes deviatoric stress. Three back-stress and two isotropic softening terms are used to capture the complex evolution and interaction of softening and hardening in the material. The Armstrong-Frederick kinematic hardening evolution equation for each back-stress,  $\boldsymbol{\chi}_i$  is as follows:

$$\dot{\boldsymbol{\chi}}_i = \frac{2}{3} C_i \dot{\boldsymbol{\varepsilon}}^p (1-D) - \gamma_i \boldsymbol{\chi}_i \dot{p} \quad (6)$$

where  $C_i$  are hardening moduli,  $\gamma_i$  are recall parameters and  $\dot{p}$  is the effective plastic strain increment. Note that total back-stress is  $\boldsymbol{\chi} = \sum \boldsymbol{\chi}_i$ . The Chaboche isotropic softening evolution with damage is calculated as follows:

$$\dot{R}_i = B_i Q_i (1-D) \dot{p} - B_i R_i \dot{p} \quad (7)$$

where  $Q_i$  are saturation stresses and  $B_i$  control the rates of saturation; also,  $R = \sum R_i$ .

### 3.2. Constitutive parameter identification

In this work a new method of constitutive model parameter identification is proposed by the authors, which accounts for the effects of damage-induced material degradation on the constitutive response during the identification process. A flowchart outlining the parameter identification procedure is shown in Figure 4. An initial set of Chaboche isotropic softening and Armstrong-Frederick kinematic hardening material parameters are first identified, following the methodology described by Barrett et al [25]. These parameters are then optimised with respect to the difference between the predicted and experimental cyclic stress-strain response for the first and half-life cycles, using the Levenberg-Marquardt algorithm in conjunction with a MATLAB uniaxial time independent cyclic plasticity code. In order to distinguish between the effects of dynamic recovery-induced softening and damage-induced softening on the constitutive response, the experimentally measured damage determined using Eq 8 is also an input to the parameter optimisation process.

$$D = 1 - \frac{\tilde{E}}{E} \quad (8)$$

where  $E$  is the initial elastic modulus and  $\tilde{E}$  is the current cyclic unloading modulus.

### 3.3. Two-stage LCF model

In this work, a new two-stage LCF damage model, which includes an early life damage term proposed by the authors and a secondary damage term based on the Lemaitre SED LCF damage model [13] is proposed. The early life damage is attributed to the formation and nucleation of microcracks in the material and will be described as primary damage henceforth. The microcracks are formed at stress concentrations and defects such as inclusions [26], and as a result of dislocation interactions at obstacles such as precipitates and high angle grain boundaries (HAGBs) ([27], [28]). The primary damage stage

represents the majority of life under a strain controlled cyclic test as shown in Figure 5. The primary damage accumulation is modelled phenomenologically as a function of accumulated plastic strain energy as follows:

$$D_{pp} = \frac{\ln(Ep^2)}{K_1 \sigma_{\max,0}^{*m_1}} \quad (9)$$

where  $\sigma_{\max,0}^*$  is the maximum damage equivalent stress during the first loading cycle,  $p$  is the accumulated effective plastic strain and  $D_{pp}$  is the primary LCF damage. The constants  $K_1$  and  $m_1$  are fitted to the experimentally observed accumulated plastic strain and damage evolutions using the least squares method. The multiaxiality of the damage model is achieved through the use of a damage equivalent stress term, which is calculated as follows:

$$\sigma^* = \sigma_{eq} \sqrt{\frac{2}{3}(1 + \nu) + 3(1 - 2\nu) \left(\frac{\sigma_H}{\sigma_{eq}}\right)^2} \quad (10)$$

where  $\sigma^*$  is the damage-equivalent stress and  $\sigma_H$  is hydrostatic stress.

The initiation criterion for the secondary damage accumulation is a function of the accumulated plastic strain and the maximum damage equivalent stress during the first loading cycle, and is given as follows:

$$p_D = \varepsilon_{pD} \left( \frac{\sigma_u - k}{\sigma_{\max,0}^* - k} \right)^n \quad (11)$$

the secondary damage accumulated plastic strain exponent  $n$  is usually assumed constant [13], but has proposed in this work as a function of the maximum damage-equivalent stress during the first loading cycle, as follows:

$$n = K_2 e^{m_2 \sigma_{\max,0}^*} \quad (12)$$

where  $\varepsilon_{pD}$  is the plastic strain damage threshold in pure tension which is obtained from a tensile test, and the parameters  $K_2$  and  $m_2$  are fitted to the experimentally observed

accumulated plastic strain at secondary damage initiation using the least squares method. The secondary damage accumulation is based on the Lemaitre SED model [13], which models the coalescence of microcracks into larger cracks along energetically favourable paths as shown in Figure 5. The secondary damage evolution is calculated as follows:

$$\frac{\delta D_{ps}}{\delta N} = \left[ \frac{\sigma_{max}^{*2}}{2ES_{PS}(1-D)^2} \right]^{m_4} \Delta p \text{ if } p > p_D \quad (13)$$

where  $S_{PS}$  is an energetic secondary LCF damage law parameter, which is also usually assumed constant, but has been proposed in this work as dependent on the maximum equivalent stress during the first loading cycle, as follows:

$$S_{PS} = K_3 \sigma_{max,0}^{*m_3} \quad (14)$$

where  $\Delta p$  is the accumulated plastic strain over one cycle,  $\sigma_{max}^*$  is the maximum value of damage-equivalent stress over one cycle and  $D_{ps}$  is secondary LCF damage. The parameters  $K_3$ ,  $m_3$  and  $m_4$  are fitted to the experimental secondary damage evolution using the least squares method.

### 3.4. NLCD HCF model

The multiaxial form of the NLCD HCF model is also used in this work to predict the stress based HCF damage accumulation. The NLCD incremental damage accumulation expression is as follows:

$$\frac{\delta D_e}{\delta N} = [1 - (1 - D)^{\beta+1}]^\alpha \left[ \frac{A_{II}}{M_0(1 - 3b_2\sigma_{H,mean})(1 - D)} \right]^\beta \quad (15)$$

where  $A_{II}$  is the amplitude of octahedral shear stress,  $\sigma_{H,mean}$  is the mean value of hydrostatic stress in a loading cycle,  $b_2$  is a parameter controlling the influence of mean hydrostatic stress and  $D_e$  is HCF or elastic regime damage. The parameter  $\alpha$  is given by:

$$\alpha = 1 - a \left\langle \frac{A_{II} - A_{II}^*}{\sigma_u - \sigma_{eq,max}} \right\rangle \quad (16)$$

where  $\sigma_{eq,max}$  is the maximum equivalent stress in a loading cycle,  $a$  is a material parameter determined from HCF tests and  $A_{II}^*$  is the Sines criterion fatigue limit [29], which is calculated as follows:

$$A_{II}^* = \sigma_{10} (1 - 3b_1 \sigma_{H,mean}) \quad (17)$$

where  $\sigma_{10}$  is the fatigue limit at fully reversed loading conditions and  $b_1$  is a parameter controlling the influence of mean hydrostatic stress.

The NLCD damage accumulation, shown in Eq 15, is dependent on an initial level of damage for a numerical solution. To provide an initial level of damage, the damage resultant from the initial cycle is calculated using the integrated form of the NLCD model, from  $D = 0$  to  $D = 1$  at  $N = N_f$ , shown in Eq 18. Under the assumption of constant amplitude cyclic loading, the linear damage accumulation per cycle for a multiaxial loading case is given by  $\frac{\delta D_e}{\delta N} = \frac{1}{N_f}$ , where:

$$N_f = \frac{1}{1 + \beta} \frac{1}{aM_0^{-\beta}} \frac{\langle \sigma_u - \sigma_{eq,max} \rangle}{\langle A_{II} - A_{II}^* \rangle} \left[ \frac{A_{II}}{1 - 3b_2 \bar{\sigma}} \right]^{-\beta} \quad (18)$$

Due to the absence of sufficient X100Q HCF experimental data for calibration of the model, in this study the parameters  $aM_0^{-\beta}$  and  $\beta$  are determined by plotting  $\ln \left( \frac{N_f \left( \frac{\Delta\sigma}{2} - \sigma_{10} \right)}{\sigma_u - \frac{\Delta\sigma}{2}} \right)$  against  $\ln \left( \frac{\Delta\sigma}{2} \right)$  as detailed by Chaudonneret [9], for S690, another Q&T steel from the same strength class using HCF test data obtained by de Jesus and co-workers [30]. The assumption of similar HCF behaviour for S690 and X100Q is justified by the close correlation of yield tensile and tensile strengths between the materials, a known indicator of HCF performance. Values previously published by Zhang et al. [11] are used for the parameters  $a$ ,  $b_1$  and  $b_2$ .

### 3.5. Combined HCF-LCF damage model

The two-stage LCF and NLCD HCF damage models are both implemented within a multiaxial NLKIH cyclic plasticity UMAT for the commercial FE solver, Abaqus. A flowchart detailing the implementation is shown in Figure 6. To determine the material damage at each integration point, the primary and secondary LCF damage are both calculated, if applicable, along with the NLCD HCF damage increment. The maximum of the damage levels predicted by these approaches at an integration point after a given loading block is then taken as the damage level for the subsequent loading block as follows:

$$(D)_j^{i+1} = \max \left\{ \frac{\delta D_e}{\delta N} \Delta N + D, \frac{\delta D_{ps}}{\delta N} \Delta N + D, D_{pp} \right\}_j^i \quad (19)$$

where  $i$  represents the current loading block,  $j$  is the number of the integration point and  $\Delta N$  is the number of fatigue cycles per loading block. The values used for  $\Delta N$  are 10,000 cycles for the 6 m wave amplitude analysis, 3,000 cycles for the 7 m analysis, 500 cycles for the 8 m analysis, 400 cycles for the 9 m analysis and 250 cycles for the 10 m analyses. Zhang and co-workers [11] have previously shown for values of  $\Delta N/N_f < 0.02$  a converged solution is obtained between the incremental and integrated NLCD models for plain fatigue specimen.

For comparative purposes, the Smith-Watson-Topper life prediction equation [18] is implemented in conjunction with the critical-plane method through Python post-processor, to predict fatigue life at the failure location of the girth weld submodel, as described by Sum and co-workers [31]. This methodology employs both the stress based Basquin [5], and plastic strain based Coffin-Manson [6] equations to form a total life equation which accounts for the effect of mean stress through peak stress and strain amplitude, as follows:

$$SWT = \sigma_{\max} \frac{\Delta \varepsilon}{2} = \frac{\sigma_f'^2}{E} (2N_f)^{2d} + \sigma_f' \varepsilon_f' (2N_f)^{d+c} \quad (20)$$

where  $SWT$  is the Smith-Watson-Topper parameter,  $\varepsilon_f'$  is the fatigue ductility coefficient  $c$  is the fatigue ductility exponent,  $\sigma_f'$  is the fatigue strength coefficient and  $d$  is the fatigue strength exponent.

### 3.6. SCR girth weld case study

The combined HCF-LCF damage UMAT subroutine is applied in combination with a global-local modelling methodology for SCR girth welds discussed in detail by Devaney et al. [4]. The dynamic multiaxial loading is obtained from the global analysis of a 3,000 m sea depth free hanging SCR in the Gulf of Mexico using a beam-element model in the offshore structural analysis FE package Flexcom [17], as shown schematically in Figure 7 (a). The SCR wall thickness required for this design is determined through a maximum stress based criteria for a series of load cases, shown in Table 2, in accordance with the API 2RD recommended practice [32]. The loading conditions analysed are representative of a combination of extreme weather conditions contained detailed in the API RP 2MET recommended practice [33], and failures in subsea infrastructure. The SCR–seabed interaction is modelled as a beam on elastic foundation, with a stiffness of 143.4 kN/m/m. Representative seabed properties obtained from the Flexcom examples manual [34] are assigned, with friction coefficients of 0.2 and 0.4 and friction stiffness's of 45 N/m/m and 90 N/m/m assigned in the longitudinal and transverse directions respectively.

Further global analyses are conducted using Airy waves at 6 m, 7 m, 8 m, 9 m and 10 m wave amplitudes. The dynamic multiaxial loading histories obtained during the global analyses are then applied to a 3D pipe section submodel in Abaqus, as shown in Figure 7 (b). The girth weld geometry used in the 3D pipe section is based on X100 welds qualified to the DNV-OS-F101 standard [35], and presented in the European FATHOMS report on

fatigue of high strength offshore welded joints [36]. The applied loading includes internal pressure, hydrostatic pressure, alternating tension, bending moment and torque arising from wave action. The pipe section model results then drive a more detailed girth weld submodel of the most highly loaded section via nodal displacement history boundary conditions, as shown inset in Figure 7 (c). Mesh convergence for the girth weld submodel is achieved with respect to the predicted maximum principal stress and the life predicted by the integrated NLCD model. In this study, the focus of attention is on the geometric effect of the weld with the X100Q parent material (PM) properties used also for the weld metal (WM) and heat affected zone (HAZ) during the analyses.

## **4. Results**

### **4.1. Experimental testing**

The bainitic microstructure of the X100Q material is shown in the optical micrograph and SEM images of Figure 8. The microstructure consists of prior austenite grain boundaries within which are regions of lower and granular bainite, which are separated by low angle boundaries (LABs).

The evolution in stress-strain response and stress amplitude observed during LCF testing is shown in Figure 9. For each of the applied strain ranges there is significant primary softening during the early cycles, which is followed by a period of stabilised secondary softening until the cycles preceding failure, where a sudden drop in stress amplitude is observed, as shown in Figure 9 (c). The Coffin-Manson relationship obtained for X100Q during LCF testing is shown in Figure 9 (d). The values of yield and yield strength and ultimate strength obtained for X100Q during tensile testing are shown in Table 3.

## 4.2. Computational modelling

The fit achieved to the experimental stress-strain response at the first cycle and half-life cycle using the proposed constitutive parameter optimisation process in combination with the two-stage LCF damage model is shown in Figure 10. There is close agreement shown between the experimental and model predicted evolutions in stress and plastic strain range for each LCF test. The full set of optimised constitutive material parameters for X100Q are shown in Table 3.

The demarcation of the experimentally observed cyclic softening into dynamic recovery and damage-induced softening for the 0.8% strain range test is shown in Figure 11. The early life damage observed for this test contributes to approximately 45 MPa of cyclic softening through the majority of the test, or approximately 30% of the softening prior to the onset of failure.

A comparison between the experimentally observed and model predicted evolution in stress-strain response for the 1% strain range test, and the evolutions in stress amplitude for all tests is shown in Figure 12. The experimentally measured damage evolutions and the damage evolutions predicted using the two-stage LCF model are shown in Figure 13. The predicted primary damage accumulation matches the early life experimental damage in each case. The predicted secondary damage accumulation is also in excellent agreement with the experimental data, and the life predictions are all within 4% of the experimental life except for the 0.7% strain range test. The identified fatigue damage model parameters for X100Q are shown in Table 4.

Multiaxial validation of the combined LCF-HCF Abaqus UMAT subroutine is achieved through the simulation of stress-controlled tests on LC4CS aluminium alloy notched specimens as detailed by Shen et al. [12], and shown in Figure 14 (b). Under a nominally elastic loading, the combined damage model successfully predicts damage-

induced plasticity and the resultant LCF damage accumulation. A comparison between the fatigue life predictions obtained using the combined damage model and the experimental results for six stress ratios is shown in Figure 14 (a), the predicted fatigue lives are all within 15% of the reported experimental lives. A contour plot of damage accumulation near failure for the 0.31 stress ratio test is shown in Figure 14 (b).

From the results of global analyses on the 3,000 m deep free hanging SCR design, using the loading conditions and the maximum von Mises stress criteria contained in Table 2, the appropriate SCR dimensions correspond to an API 12 inch SCH 140 pipe section with an outer diameter of 323.8 mm and a wall thickness of 28.6 mm. An additional insulation coating of thickness 63.5 mm is assumed for hydrodynamic drag purposes during the global analyses. The hang-off zone, below the floating production storage and offloading facility (FPSO) was determined to be the critical region in terms of fatigue performance. Due to the high tension in this region from the suspended mass of the SCR, the hang-off zone consistently exhibited highest peak stress and alternating stress range. The fatigue lives predicted for a girth weld in this location using the combined two-stage LCF-HCF, integrated NLCD and the critical-plane SWT models during Abaqus submodel analyses are shown in Figure 15. The integrated NLCD and critical-plane SWT models predictions are based on the first cycle stress-strain range. A contour plot of the damage accumulation predicted at failure using the combined two-stage LCF-HCF combined damage model for the 7 m wave amplitude load case is shown in Figure 16. The damage and accumulated plastic strain evolutions at the location of failure in the weld toe for this load case is shown in Figure 17.

## 5. Discussion

### 5.1. Experimental testing

The X100Q material displayed LCF performance in agreement with that of the S690 steel tested by de Jesus et al. [30], in terms of the relationship between applied strain range and life. However, the X100Q exhibited significant cyclic softening, in contrast to the S690 material which showed a small level of hardening. Due to this cyclic softening, the plastic strain range also cyclically increased. As a result the material exhibited superior LCF performance in terms of the Coffin-Manson relationship when compared to S690. The cyclic softening exhibited by the X100Q material is primarily attributed to the onset of the dynamic recovery process, leading to the annihilation and rearrangement of dislocations and the removal of dislocation pinning, as reported by Lucas et al. [37] and Sankaran et al [38] for Q&T steels. However, when the early life damage is taken into consideration as in Figure 11, it is clear that damage makes a significant contribution to the observed cyclic softening for the material. This early life damage is attributed to the formation of microcracks at defects such as inclusions, and the dislocation interactions which occur due to dislocation pile-up at obstacles, such as HAGBs and precipitates. Microcracking at grain boundaries due to dislocation pile-up has been previously discussed in the literature, for example by Tanaka [39], Hu [27] and Hamada [40]. Majumdar and co-workers [28] also reported early life initiation of grain boundary microcracks and the resultant intergranular crack growth in a fine-grained low alloy steel. Intuitively it is not surprising that X100Q may be susceptible to early life damage due to the formation of microcracks, as a result of its high dislocation and grain boundary density. This is also in agreement with the relation derived by Tanaka [39], which relates the number of cycles to microcrack initiation to the cube of the grain size. Observations of surface short crack growth by Polák [41] for a quenched and tempered low alloy steel with a bainitic-ferritic-pearlitic microstructure also show surface fatigue crack (damage)

initiation at under 5 to 10% of total life, and that the density of microcracks increased with plastic strain amplitude, which is in agreement with the increasing level of early life damage observed in this work for higher strain ranges. It was noted that for the 0.7% strain range test that the knife edge leg of the extensometer interfered with the fatigue crack path. This is likely to have caused premature failure of the specimen and can be confirmed objectively by comparing the fatigue lives of the 0.8%, 0.7%, and 0.6% strain range tests.

## **5.2. Computational modelling**

The extent to which the early life damage observed for X100Q during the LCF test programme contributes to the experimental cyclic softening calls into question the validity of the standard approach of fitting constitutive models to half-life data for similar materials, under the assumption that the material damage accumulation is negligible to the half-life cycle. When fitting a constitutive model in this manner to a material exhibiting early life damage, it is likely that the extent of isotropic hardening will be underestimated, or isotropic softening will be overestimated.

The combined application of the constitutive model parameter optimisation process accounting for experimental damage and the two-stage LCF damage model gives excellent agreement with the experimental stress-strain response and fatigue damage behaviour observed for X100Q as shown in Figures 12 and 13 respectively. In particular, the predicted primary damage accumulation shown in Figure 13 matches the experimentally observed damage accumulation to a high degree of accuracy. The proportionality between primary damage and accumulated plastic strain proposed in the primary damage model of Eq 9 is also in agreement with observations made by Polák on the proportionality between the logarithm of surface crack (damage) length and fatigue cycles for a constant plastic strain amplitude test. The life and secondary damage

accumulation predictions are also in close agreement with the experimental observations, for all but the 0.7% strain range test due to an experimental anomaly. However, the predictions made by the two-stage LCF damage model in Figure 13 appear to give a plausible failure point for the 0.7% strain range test.

The combined LCF-HCF damage Abaqus UMAT subroutine is shown to successfully predict multiaxial fatigue failure and the damage-induced plasticity phenomenon through validation against notched LC4CS aluminium alloy test data for a variety of stress ratios. In relation to the case study on fatigue at an SCR girth weld, the fatigue lives predicted by the combined LCF-HCF and the integrated NLCD damage models are conservative with respect to the critical-plane SWT at high wave amplitudes. This is most likely due to the fact the critical-plane SWT model is essentially a uniaxial fatigue model, which only accounts for the influence of loading on the determined critical plane, and as the model does not use an incremental approach the evolution in stress-strain response and the effect of damage is neglected. The conservatism in the integrated NLCD model life predictions with respect to combined LCF-HCF model may also be attributed to the inability of the model to account for the evolution in stress-strain response resultant from damage and plasticity.

The high fatigue lives predicted by the combined damage model under severe loading conditions indicate conservatism in the weld design. Assuming a constant wave amplitude and period, the predicted life for the 7 m wave amplitude case equates to almost 5 months of constant weather equivalent to a 10-year winter storm before the initiation of fatigue the depth of an integration point, approximately 0.56 mm. It can be seen from Figure 16 that the influence of weld geometry alone results in a significant concentration of damage at the weld toe. The concentration of damage and the associated material degradation in this region results in a significant accumulation of plastic strain, as shown

in Figure 17. However, the modelling conducted in this study did not account for potential weld defects, the inhomogeneity of the weldment zone or residual stress, which are likely to have a significant detrimental effect on fatigue life. Future work will address these omissions by experimental characterisation of the HAZ and WM, and through process modelling of the SCR girth weld to obtain a realistic microstructure and residual stress distribution.

The applicability of the combined HCF-LCF fatigue analysis methodology described here extends beyond offshore pipelines and structures. For large structures such as SCRs a compromise between accuracy and computational cost can be achieved by conducting global analyses for initial design purposes using a total life approach, then conducting more detailed analyses at regions which have been identified as hot-spots using the combined HCF-LCF fatigue analysis methodology.

## **6. Conclusions**

In this work, the LCF and plasticity behaviour of X100Q has been experimentally characterised and modelled. A new LCF damage model and associated parameter optimisation procedure has been developed, the model was calibrated and validated against X100Q LCF test data. The new LCF model was then applied to the computational case study of damage accumulation in an SCR girth weld. Key conclusions from this work are as follows:

- During LCF testing of the X100Q significant cyclic softening behaviour was observed. This has been attributed to a combination of dynamic recovery and damage-induced softening as a result of dislocation interactions in the fine-grained dislocation dense material.
- The significant contribution of damage to the observed cyclic softening in X100Q highlights the importance of demarcating microstructural recovery-induced

softening from damage-induced softening, to accurately model the material behaviour.

- The combined application of the proposed constitutive parameter identification process and two-stage LCF model provides excellent agreement with the experimentally observed behaviour for X100Q in terms of constitutive response, damage accumulation and life prediction.
- A combined LCF-HCF damage mechanics model has been successfully implemented within an Abaqus UMAT subroutine. The model has been validated against multiaxial test data through notched specimen simulations.
- The new damage model has been applied to a computational case study on an X100Q SCR girth weld geometry designed in accordance with recommended industrial practices. The fatigue life predicted by the combined LCF-HCF damage model is in close agreement with the integrated NLCD model, but is conservative when compared to the predictions of the critical-plane SWT model. The model successfully predicts the influence of weld geometry and damage-induced plasticity on the fatigue life of an SCR girth weld.

## **7. Acknowledgements**

This publication has emanated from research conducted with the financial support of Science Foundation Ireland as part of the MECHANNICS joint project between NUI Galway and University of Limerick under Grant Number SFI/14/IA/2604.

The authors would also like to thank Dr. Adrian Connaire of Wood PLC for his advice and support in providing the Flexcom software used in this publication, and the Irish centre for high-end computing (ICHEC) for provision of computational resources used in this work.

## Nomenclature

- $a$  - NLCD model parameter controlling mean stress effect
- $A_{II}$  - Amplitude of octahedral shear stress
- $A_{II}^*$  - Sines criterion fatigue limit
- $\beta$  -HCF material constant
- $b_1$  - Parameter controlling influence of mean hydrostatic stress on Sines fatigue limit
- $b_2$  - Parameter controlling influence of mean hydrostatic stress on HCF damage
- $C_i$  - Armstrong-Frederick kinematic hardening moduli
- $B_i$  - Isotropic softening rate controlling parameters
- $D$  - Isotropic damage level
- $D_{pp}$  - Primary LCF damage
- $D_{ps}$  - Secondary LCF damage
- $D_e$  - HCF damage
- $\Delta N$  - Number of cycles in a fatigue loading block
- $E$  - Undamaged or initial elastic modulus
- $\tilde{E}$  - Effective elastic modulus due to damage
- $\boldsymbol{\varepsilon}^e$  - Elastic strain tensor
- $\dot{\boldsymbol{\varepsilon}}^p$  - Increment in plastic strain tensor
- $f$  - Yield function
- $\gamma_1$  - Armstrong-Frederick kinematic hardening recall parameters
- $k$  - Cyclic yield stress
- $K_1$  - Fitted primary LCF damage constant
- $K_2$  - Fitted constant for secondary LCF damage initiation
- $K_3$  - Fitted constant for secondary LCF damage parameter  $S_{ps}$
- $\dot{\lambda}$  - Plastic multiplier
- $M_0$  - HCF constant
- $m_1$  - Fitted primary LCF damage exponent
- $m_2$  - Fitted exponent for secondary LCF damage initiation
- $m_3$  - Fitted exponent for secondary LCF damage parameter  $S_{ps}$
- $m_4$  - Fitted exponent for secondary LCF damage accumulation
- $N_f$  - Number of fatigue cycles to failure
- $n$  - Secondary LCF damage accumulated plastic strain exponent

$p$  - Effective plastic strain  
 $p_D$  - Accumulated plastic strain at onset of secondary LCF damage  
 $\dot{p}$  - Increment in effective plastic strain  
 $Q_i$  - Isotropic softening saturation stresses  
 $R$  - Total isotropic softening term  
 $\dot{R}_i$  - Increment in isotropic softening term  $R_i$   
 $S$  - Area of material on a plane perpendicular to the direction  $\vec{n}$   
 $S_D$  - Area of material voids in  $S$   
 $S_{PS}$  - Energetic secondary LCF damage law parameter  
 $\tilde{S}$  - Effective load resisting area perpendicular to the direction  $\vec{n}$   
 $\sigma$  - Stress tensor  
 $\sigma_{eq}$  - von Mises equivalent stress  
 $\sigma_{eq,max}$  - Maximum von Mises equivalent stress in a loading cycle  
 $\sigma_H$  - Hydrostatic stress  
 $\sigma_{H,mean}$  - Mean value of hydrostatic stress in a loading cycle  
 $\sigma_{l0}$  - Fatigue limit under fully reversed loading  
 $\sigma_u$  - Ultimate tensile strength  
 $\sigma^*$  - Damage equivalent stress  
 $\sigma_{max,0}^*$  - Maximum damage equivalent stress during the first loading cycle  
 $\tilde{\sigma}$  - Effective stress  
 $\text{Tr}(\sigma)$  - Trace of the stress tensor  
 $\nu$  - Poisson's ratio  
 $\chi$  - Total Armstrong-Frederick kinematic backstress tensor  
 $\dot{\chi}_i$  - Increment in kinematic backstress tensor  $\chi_i$

## References

- [1] D. B. Rosado, W. D. Waele, D. Vanderschueren, and S. Hertelé, “Latest developments in mechanical properties and metallurgical features of high strength line pipe steels,” *Int. J. Sustain. Constr. Des.*, vol. 4, no. 1, p. 10, 2013.
- [2] A. Reda, I. A. Sultan, I. M. Howard, G. L. Forbes, and K. K. McKee, “Pipeline walking and anchoring considerations in the presence of riser motion and inclined seabed,” *Int. J. Press. Vessel. Pip.*, vol. 162, no. January, pp. 71–85, 2018.
- [3] “Recommended Practice DNV-RP-F204 Riser Fatigue.” Oslo, p. 34, 2010.
- [4] R. J. Devaney, P. E. O’Donoghue, and S. B. Leen, “Global and local fatigue analysis of X100 and X60 steel catenary riser girth welds,” *J. Struct. Integr. Maint.*, vol. 2, no. 3, pp. 181–189, Jul. 2017.
- [5] O. H. Basquin, “The exponential law of endurance tests,” *Proc. ASTM*, vol. 10, pp. 625–630, 1910.
- [6] L. F. Coffin, “A Study of the Effects of Cyclic Thermal Stresses on a Ductile Metal,” *ASME Trans.*, vol. 76, pp. 931–950, 1954.
- [7] S. S. Manson, “Behavior Of Materials Under Conditions Of Thermal Stress,” *NACA Rep. 1170*, pp. 317–350, 1953.
- [8] J. L. Chaboche and P. M. Lesne, “A non-linear continuous fatigue damage model,” *Fatigue Fract. Eng. Mater. Struct.*, vol. 11, no. 1, pp. 1–17, 1988.
- [9] M. Chaudonneret, “A Simple and Efficient Multiaxial Fatigue Damage Model for Engineering Applications of Macro-Crack Initiation,” *J. Eng. Mater. Technol.*, vol. 115, no. 4, p. 373, 1993.
- [10] A. K. Marmi, A. M. Habraken, and L. Duchene, “Multiaxial fatigue damage modelling at macro scale of Ti – 6Al – 4V alloy,” *Int. J. Fatigue*, vol. 31, no. 11–

- 12, pp. 2031–2040, 2009.
- [11] T. Zhang, P. E. McHugh, and S. B. Leen, “Finite element implementation of multiaxial continuum damage mechanics for plain and fretting fatigue,” *Int. J. Fatigue*, vol. 44, pp. 260–272, 2012.
- [12] F. Shen, G. Z. Voyiadjis, W. Hu, and Q. Meng, “Analysis on the fatigue damage evolution of notched specimens with consideration of cyclic plasticity,” *Fatigue Fract. Eng. Mater. Struct.*, vol. 38, pp. 1194–1208, 2015.
- [13] J. Lemaitre and R. Desmorat, *Engineering Damage Mechanics*. Berlin, 2005.
- [14] M. Sauzay, H. Brillet, I. Monnet, M. Mottot, F. Barcelo, B. Fournier, and A. Pineau, “Cyclically induced softening due to low-angle boundary annihilation in a martensitic steel,” *Mater. Sci. Eng. A*, vol. 400–401, no. 1–2 SUPPL., pp. 241–244, Jul. 2005.
- [15] M. Sauzay, B. Fournier, M. Mottot, A. Pineau, and I. Monnet, “Cyclic softening of martensitic steels at high temperature—Experiments and physically based modelling,” *Mater. Sci. Eng. A*, vol. 483–484, no. 1–2 C, pp. 410–414, Jun. 2008.
- [16] R. A. Barrett, P. E. O’Donoghue, and S. B. Leen, “A physically-based constitutive model for high temperature microstructural degradation under cyclic deformation,” *Int. J. Fatigue*, vol. 100, pp. 388–406, Jul. 2017.
- [17] *Flexcom Version 8.4.1 Software Documentation*. Galway: Wood Group Kenny, 2015.
- [18] K. N. Smith, P. Watson, and T. H. Topper, “A stress-strain function for the fatigue of metals,” *J. Mater.*, vol. 5, no. 4, pp. 767–778, 1970.
- [19] API Specification 5L and ISO 3183, “Specification for Line Pipe,” 2012.
- [20] ASTM, “Standard Test Methods for Tension Testing of Metallic Materials,” *E8/E8M-16a*, no. 16a, pp. 1–27, 2016.

- [21] S. T. Method, “ASTM E606/E606M Standard test method for strain controlled fatigue testing,” no. September. American Society for Testing and Materials, 2012.
- [22] L. M. Kachanov, “On the Time to Failure under Creep Conditions,” *Izv. Ak. Nauk USSR Otd. Tekh. Nauk*, vol. 8, pp. 26–31, 1958.
- [23] Y. N. Rabotnov, “Creep Rupture,” in *Applied Mechanics Conference*, 1968, pp. 342–349.
- [24] J. L. Chaboche, “Time-independent constitutive theories for cyclic plasticity,” *Int. J. Plast.*, vol. 2, no. 2, pp. 149–188, Jan. 1986.
- [25] R. A. Barrett, E. M. O’Hara, P. E. O’Donoghue, and S. B. Leen, “High-Temperature Low-Cycle Fatigue Behavior of MarBN at 600 °C,” *J. Press. Vessel Technol.*, vol. 138, no. 4, p. 41401, 2016.
- [26] S. Suresh, *Fatigue of Materials*. Cambridge: Cambridge University Press, 1998.
- [27] X. Hu, L. Huang, W. Yan, W. Wang, W. Sha, Y. Shan, and K. Yang, “Low cycle fatigue properties of CLAM steel at 823 K,” *Mater. Sci. Eng. A*, vol. 613, pp. 404–413, Sep. 2014.
- [28] S. Majumdar, D. Bhattacharjee, and K. K. Ray, “On the Micromechanism of Fatigue Damage in an Interstitial-Free Steel Sheet,” *Metall. Mater. Trans. A*, vol. 39, no. 7, pp. 1676–1690, Jul. 2008.
- [29] G. Sines, “Behaviour of metals under complex static and alternating stresses, technical note 3495,” 1955.
- [30] A. M. P. de Jesus, R. Matos, B. F. C. Fontoura, C. Rebelo, L. Simões da Silva, and M. Veljkovic, “A comparison of the fatigue behavior between S355 and S690 steel grades,” *J. Constr. Steel Res.*, vol. 79, no. December 2012, pp. 140–150, Dec. 2012.

- [31] W. S. Sum, E. J. Williams, and S. B. Leen, "Finite element, critical-plane, fatigue life prediction of simple and complex contact configurations," *Int. J. Fatigue*, vol. 27, no. 4, pp. 403–416, Apr. 2005.
- [32] "API RP 2RD: Design of Risers for Floating Production Systems (FPSs) and Tension-Leg Platforms (TLPs)," American Petroleum Institute, 1998.
- [33] "API RP 2MET: Derivation of Metocean Design and Operating Conditions." American Petroleum Institute, 2014.
- [34] *Flexcom Version 8.4.1 Examples Manual*. Galway: Wood Group Kenny, 2015.
- [35] "DNV-OS-F101: Submarine Pipeline Systems." Det Norske Veritas AS, p. 367, 2013.
- [36] E. Mecozzi, M. Lecca, S. Sorrentino, M. Large, C. Davies, H. Gouveia, C. Maia, M. Erdelen-Peppler, S. Karamanos, and P. Perdikaris, "EUR 24214 - Fatigue behaviour of high-strength steel-welded joints in offshore and marine systems (FATHOMS)," Luxembourg, 2010.
- [37] J. Lucas and W. Gerberich, "Cyclic strain hardening of polygonal and acicular ferrite/bainite microstructures in microalloyed steels in the temperature range – 150°C to 27°C," *Int. J. Fatigue*, vol. 7, no. 1, pp. 31–38, Jan. 1985.
- [38] S. Sankaran, V. S. Sarma, and K. a Padmanabhan, "Low cycle fatigue behavior of a multiphase microalloyed medium carbon steel : comparison between ferrite/pearlite and quenched and tempered microstructures," *Mater. Sci. Eng. A*, vol. 345, pp. 328–335, 2003.
- [39] K. Tanaka and T. Mura, "A Dislocation Model for Fatigue Crack Initiation," *J. Appl. Mech.*, vol. 48, no. 1, p. 97, 1981.
- [40] A. S. Hamada, L. P. Karjalainen, and J. Puustinen, "Fatigue behavior of high-Mn TWIP steels," *Mater. Sci. Eng. A*, vol. 517, no. 1–2, pp. 68–77, Aug. 2009.

- [41] J. Polák, “Plastic strain-controlled short crack growth and fatigue life,” *Int. J. Fatigue*, vol. 27, no. 10–12, pp. 1192–1201, Oct. 2005.

Table 1. The reported chemical composition of the as-received X100Q steel (% wt).

<b>C</b>	<b>Si</b>	<b>Mn</b>	<b>P</b>	<b>S</b>	<b>Al</b>	<b>B</b>
0.14	0.21	1.17	0.008	0.001	0.084	0.0025
<b>Cr</b>	<b>Cu</b>	<b>Mo</b>	<b>N</b>	<b>Nb</b>	<b>Ni</b>	<b>Ti</b>
0.32	0.01	0.3	0.004	0.027	0.02	0.005

Table 2. The global analysis load case matrix used to determine the required SCR wall thickness.

<b>Load category</b>	<b>Environment</b>	<b>Internal Pressure (MPa)</b>	<b>Maximum allowable stress (MPa)</b>
<b>Operating</b>	10-year winter storm	24	$0.67\sigma_y$
<b>Extreme</b>	100-year hurricane	2	$0.8\sigma_y$
<b>Survival</b>	100-year hurricane	86	$\sigma_y$
<b>Robustness</b>	1000-year hurricane	2	$\sigma_y$

Table 3. The constitutive parameters identified for X100Q.

<b>Parameter</b>	<b>Value</b>
<b><math>E</math> (GPa)</b>	209.84
<b><math>\nu</math></b>	0.3
<b><math>\sigma_{y0.2\%}</math> (MPa)</b>	783
<b><math>k</math> (MPa)</b>	279.45
<b><math>\sigma_u</math> (MPa)</b>	927
<b><math>B_1</math></b>	0.0104
<b><math>Q_1</math> (MPa)</b>	-181.79
<b><math>B_2</math></b>	0.3912
<b><math>Q_2</math> (MPa)</b>	-68.21
<b><math>C_1</math> (GPa)</b>	1200.68
<b><math>\gamma_1</math></b>	4562.32
<b><math>C_2</math> (GPa)</b>	359.95
<b><math>\gamma_2</math></b>	2858.68
<b><math>C_3</math> (GPa)</b>	94.69
<b><math>\gamma_3</math></b>	32.66

Table 4. The fatigue damage parameters identified for X100Q.

<b>Parameter</b>	<b>Value</b>
$\sigma_{10}$ (MPa)	223
$\sigma_f'$ (MPa)	1403
$d$	-0.087
$\varepsilon_f'$	0.7314
$c$	-0.681
$\beta$	8.96
$\alpha M_0^{-\beta}$	$2.229 \times 10^{-30}$
$b_1$ (MPa <sup>-1</sup> )	0.0013
$b_2$ (MPa <sup>-1</sup> )	0.00055
$a$	0.75
$K_1$	$2 \times 10^{12}$
$m_1$	-3.504
$K_2$	0.6938
$m_2$	0.038
$K_3$	$4.7886 \times 10^{-7}$
$m_3$	2.2953
$m_4$	20
$\varepsilon_{pD}$	0.345
$n$	1.19

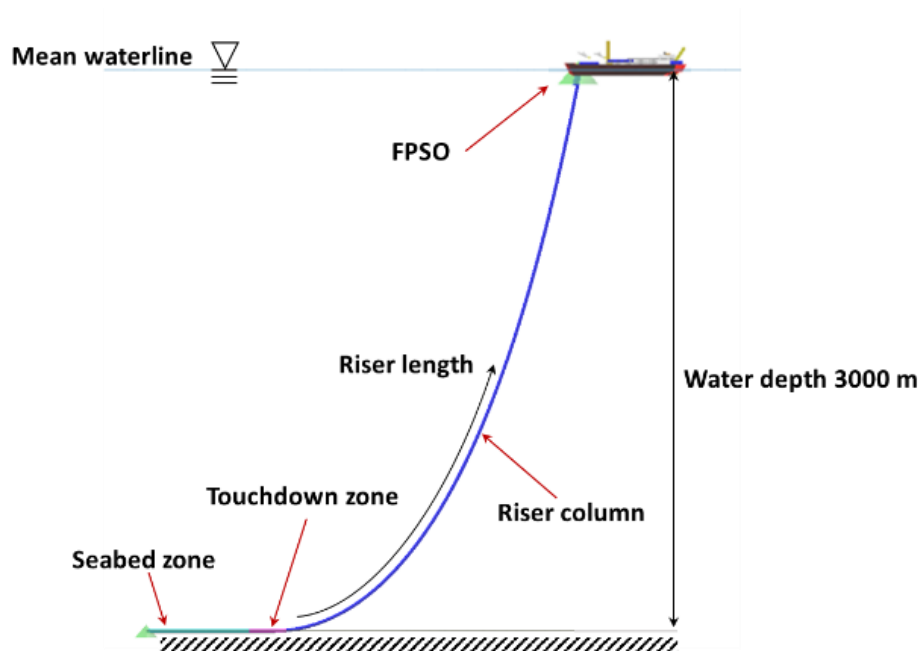


Figure 1. Schematic diagram of a free hanging SCR connected to a floating production storage and offloading vessel (FPSO).

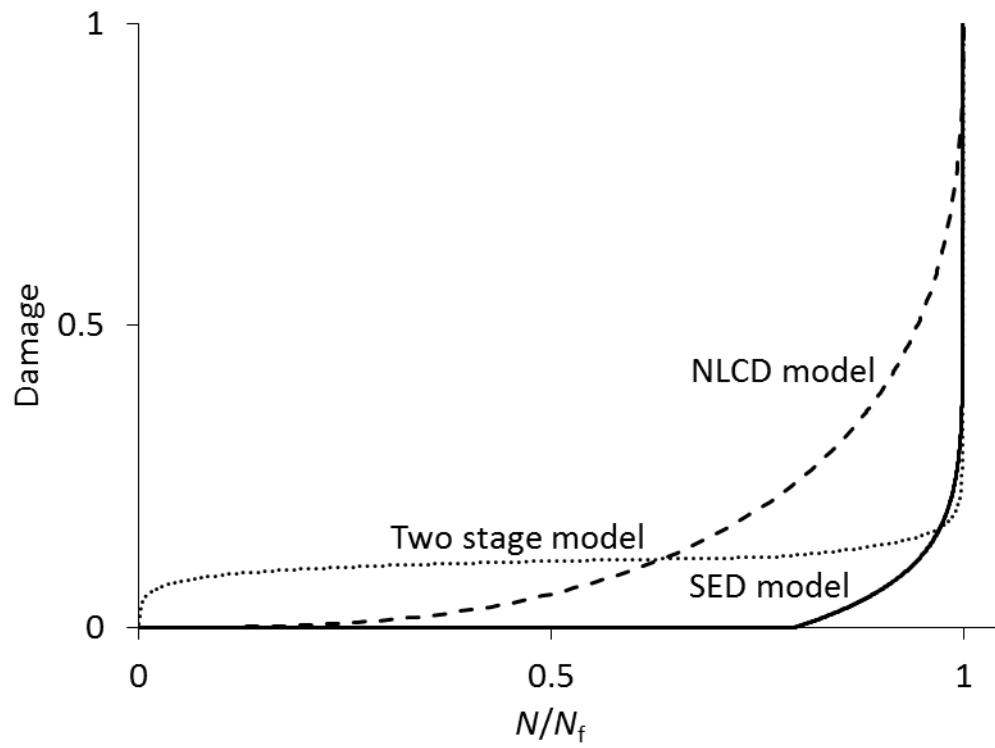


Figure 2. Comparison between the typical damage evolutions predicted by the NLCD model, the SED model, and the proposed two-stage model.

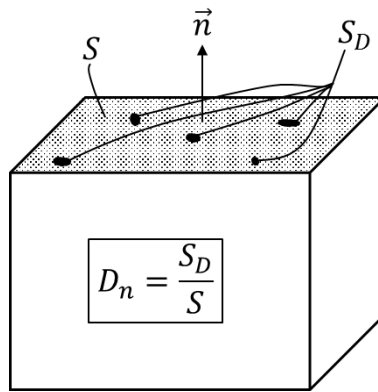


Figure 3. Material element highlighting the reduction in load resisting area due to damage.

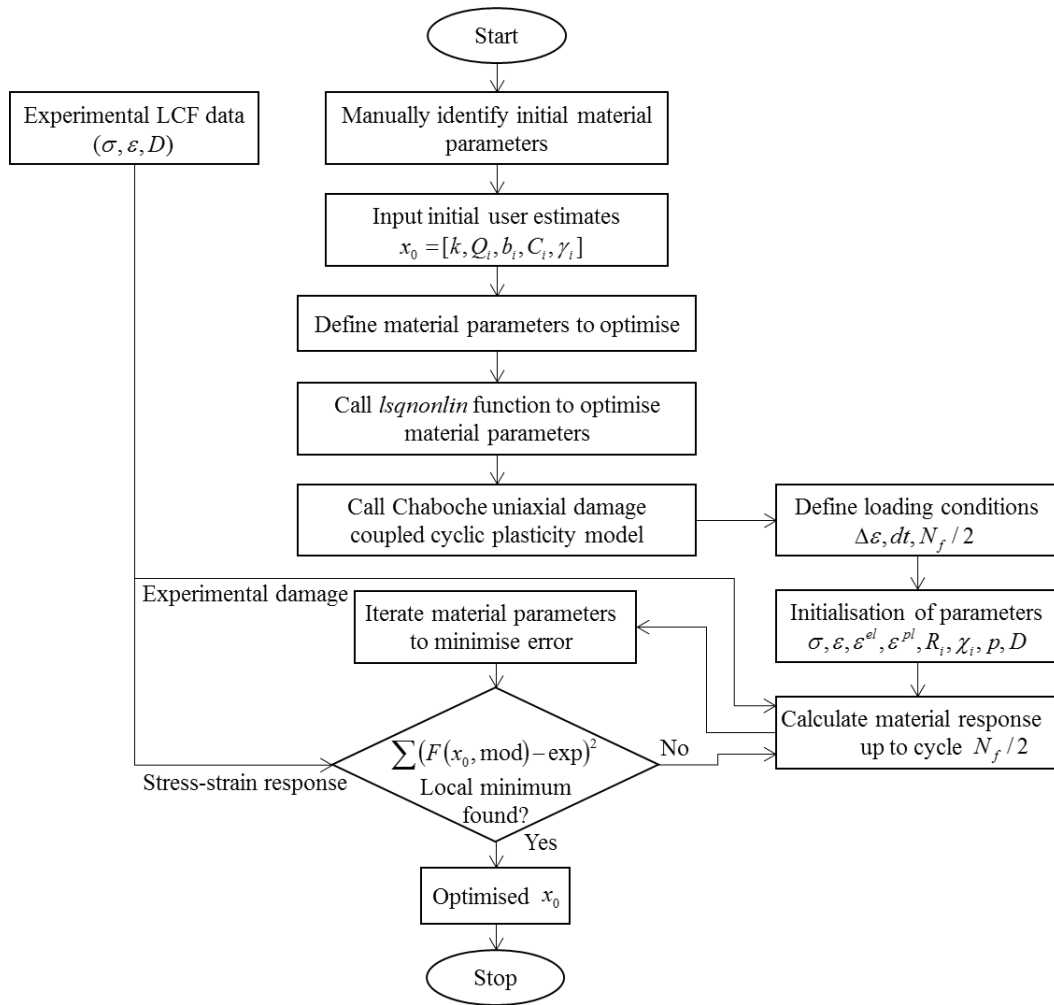


Figure 4. Flowchart of the proposed constitutive parameter identification and optimisation process.

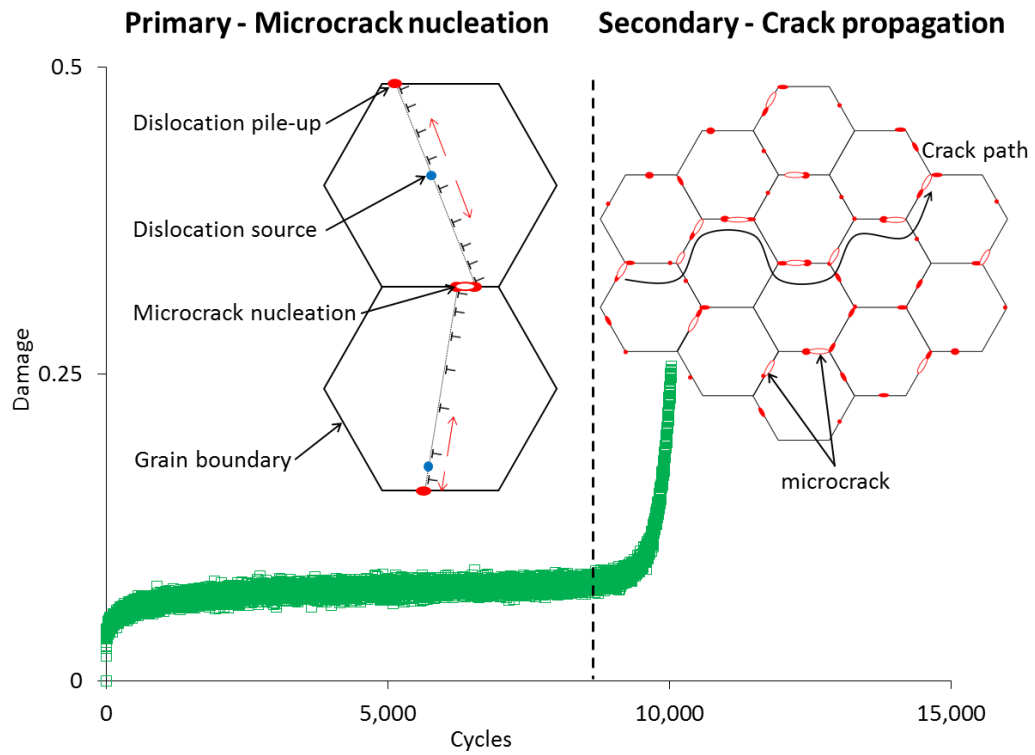


Figure 5. The experimentally measured damage accumulation from the 0.8% strain range test with schematic images of the key damage mechanisms during the primary and secondary stages.

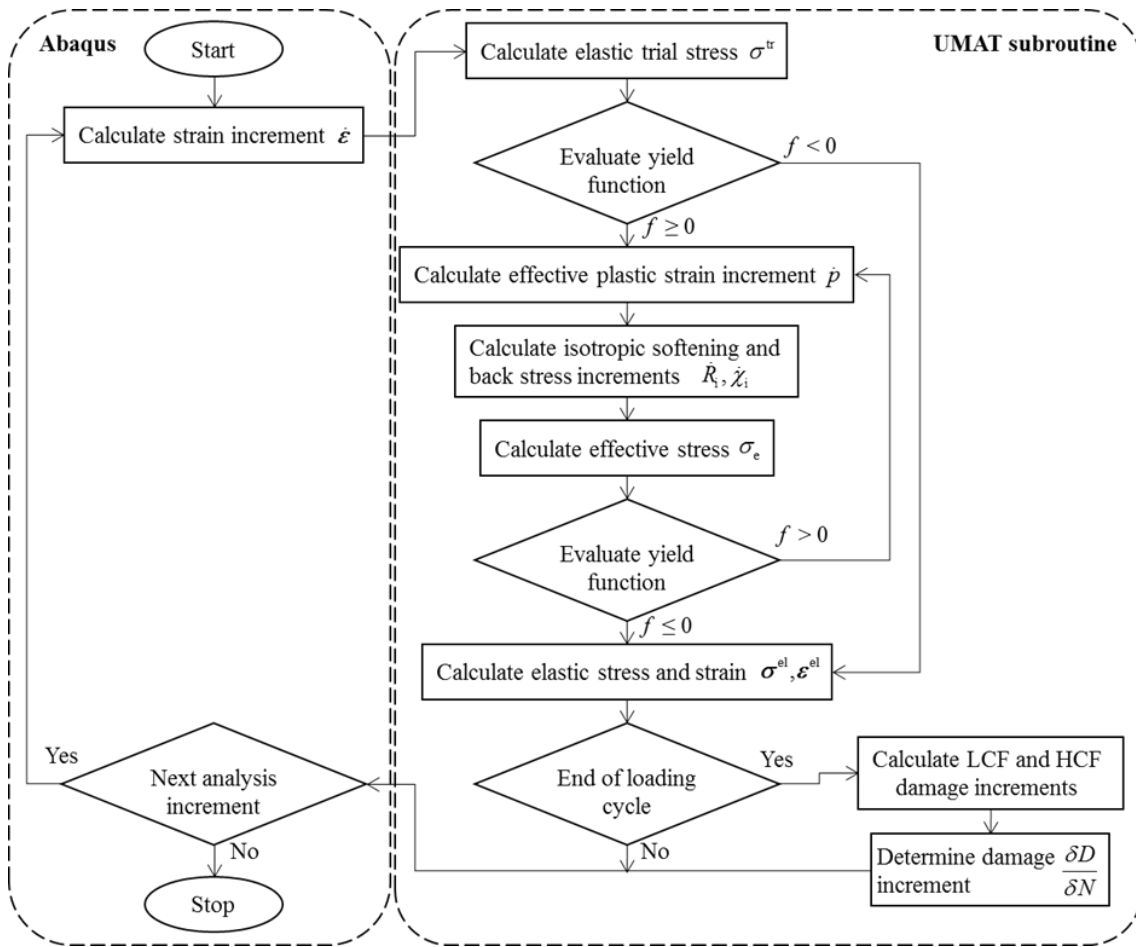


Figure 6. Flowchart of the combined fatigue damage model implementation within an Abaqus cyclic plasticity UMAT subroutine.

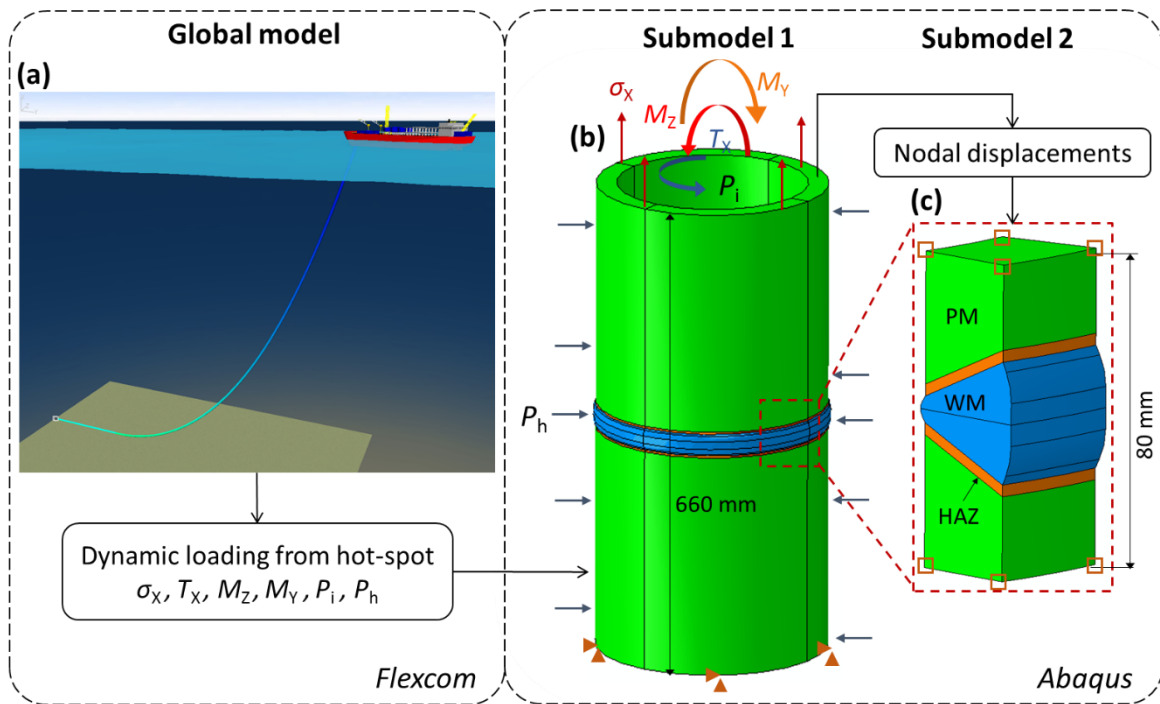


Figure 7. Schematic image detailing the global-local SCR modelling methodology, with (a) a freehanging SCR Flexcom global model, (b) a 3D pipe section and (c) detailed weld section submodels.

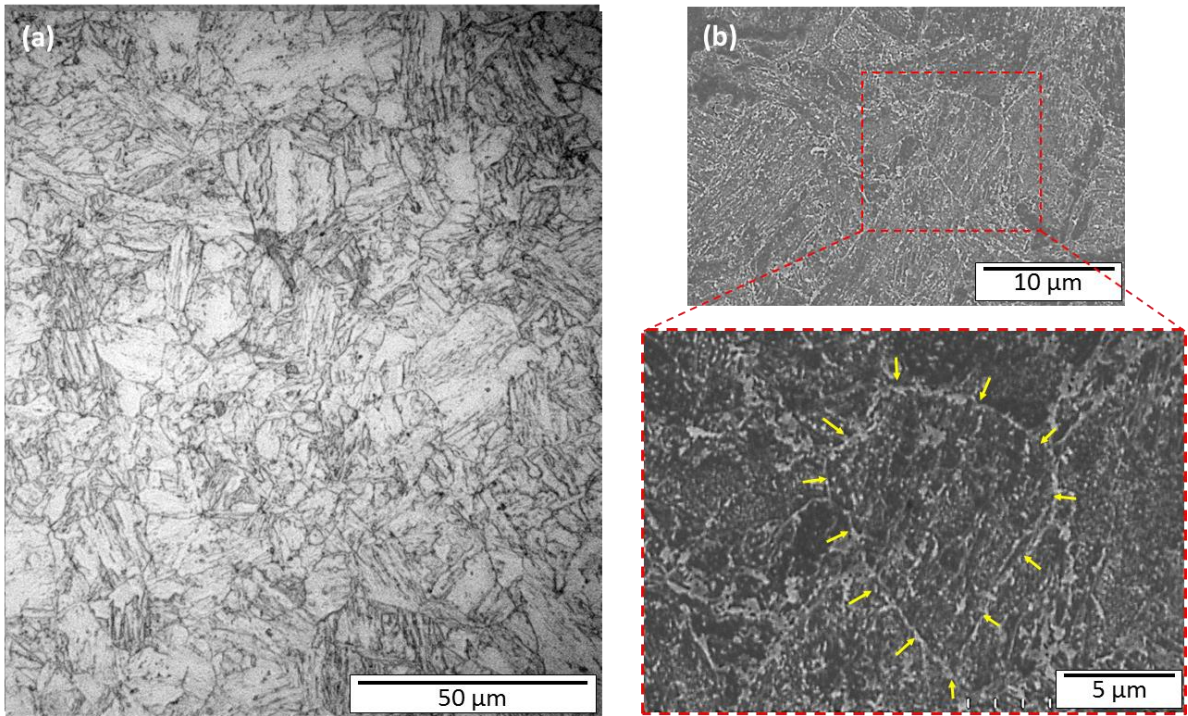


Figure 8. (a) Optical micrograph of the X100Q microstructure and (b) SEM image of the X100Q microstructure with prior austenite grain boundary highlighted (yellow arrows).

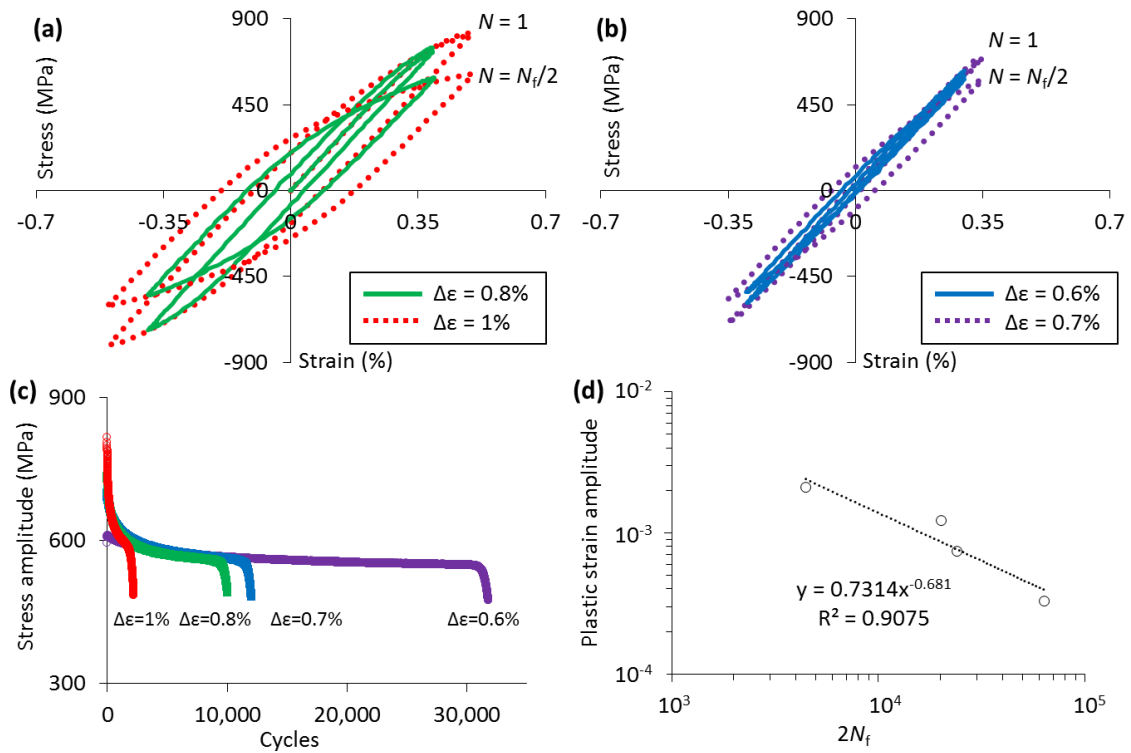


Figure 9. The measured cyclic stress-strain response for the (a) 1% and 0.8%, and (b) 0.7% and 0.6% strain range tests. Also, evolution of the (c) measured stress amplitude and (d) the observed Coffin-Manson relationship.

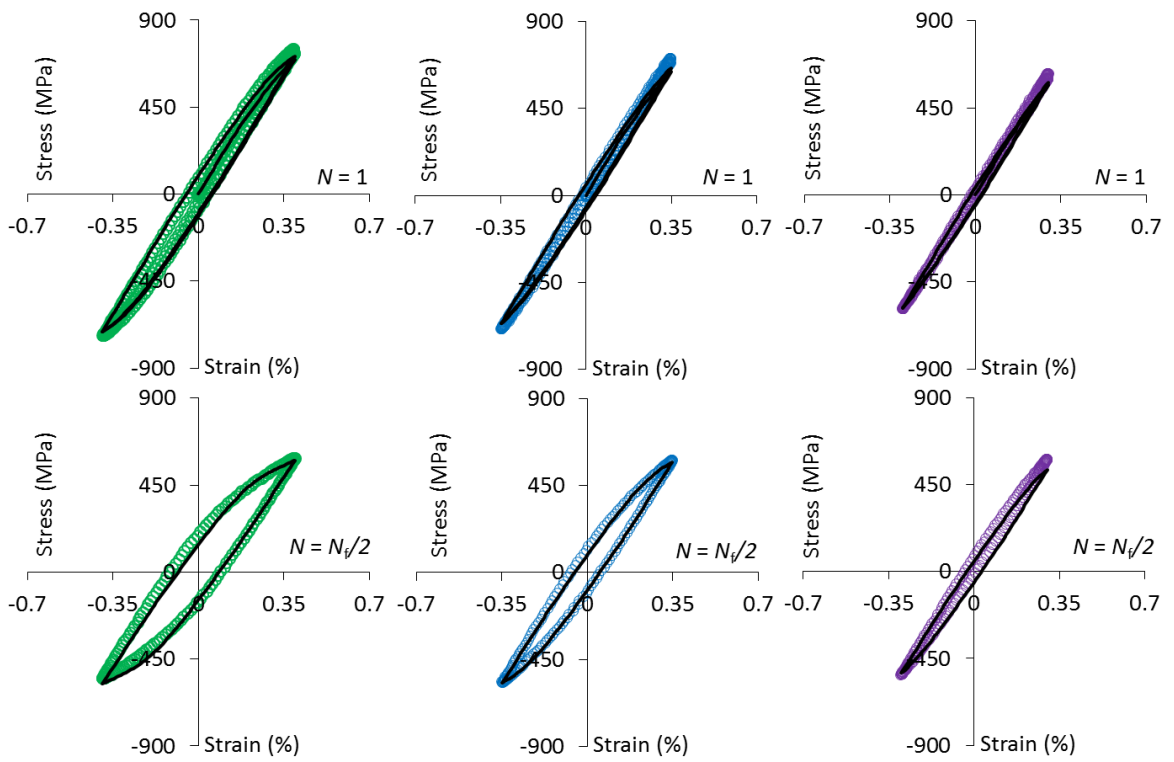


Figure 10. The fit achieved between the experimentally measured (open symbols) and model-predicted (lines) stress-strain responses at the first and half-life cycles for the 0.8%, 0.7%, and 0.6% strain range tests.

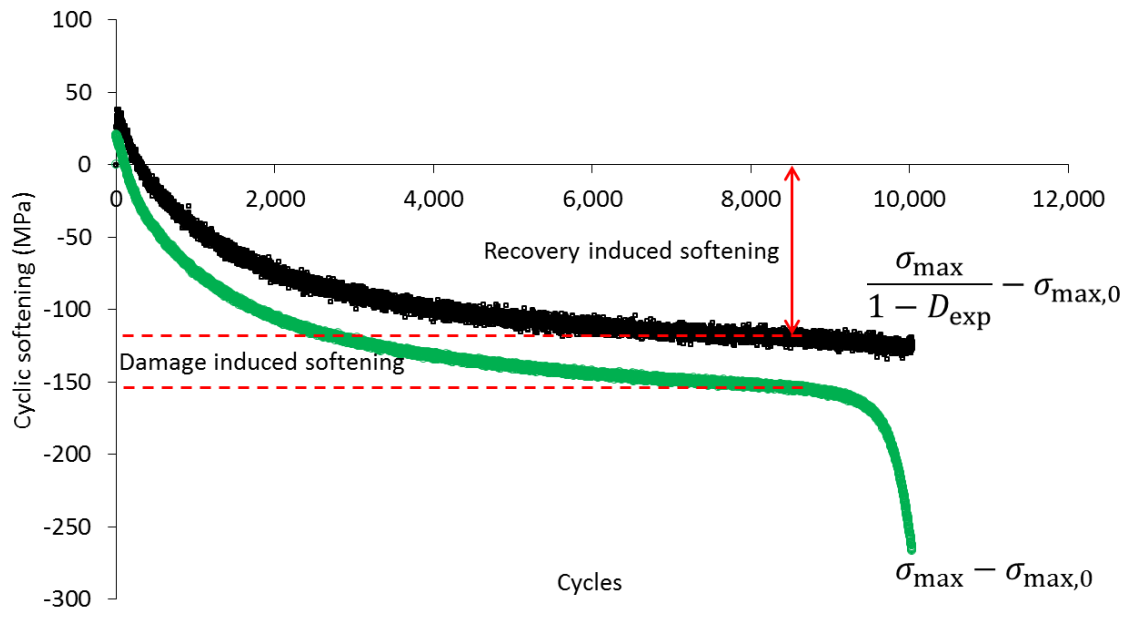


Figure 11. A plot of cyclic softening detailing the quantification of the recovery and damage-induced softening for the 0.8% strain range test.

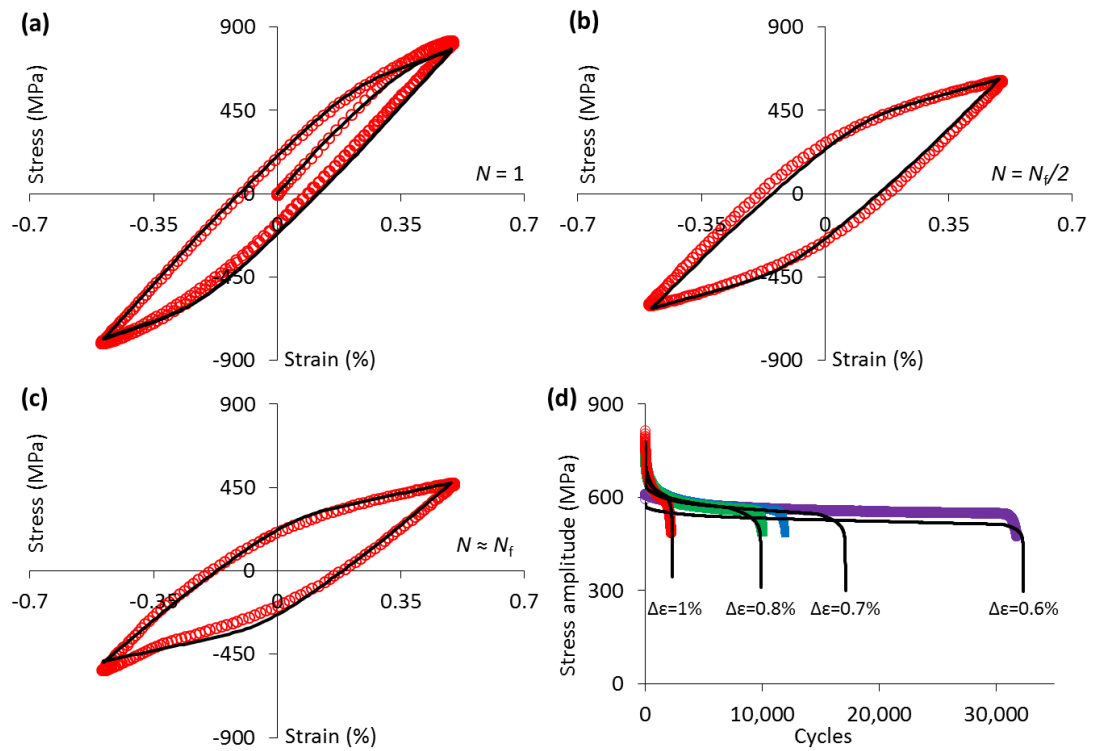


Figure 12. The fit achieved between the experimental evolution (open symbols) in stress-strain response and the model (lines) for the (a) first cycle, (b) half-life cycle, (c) final cycle and (d) stress amplitude evolution using the constitutive parameter identification process accounting for damage and the two-stage LCF model.

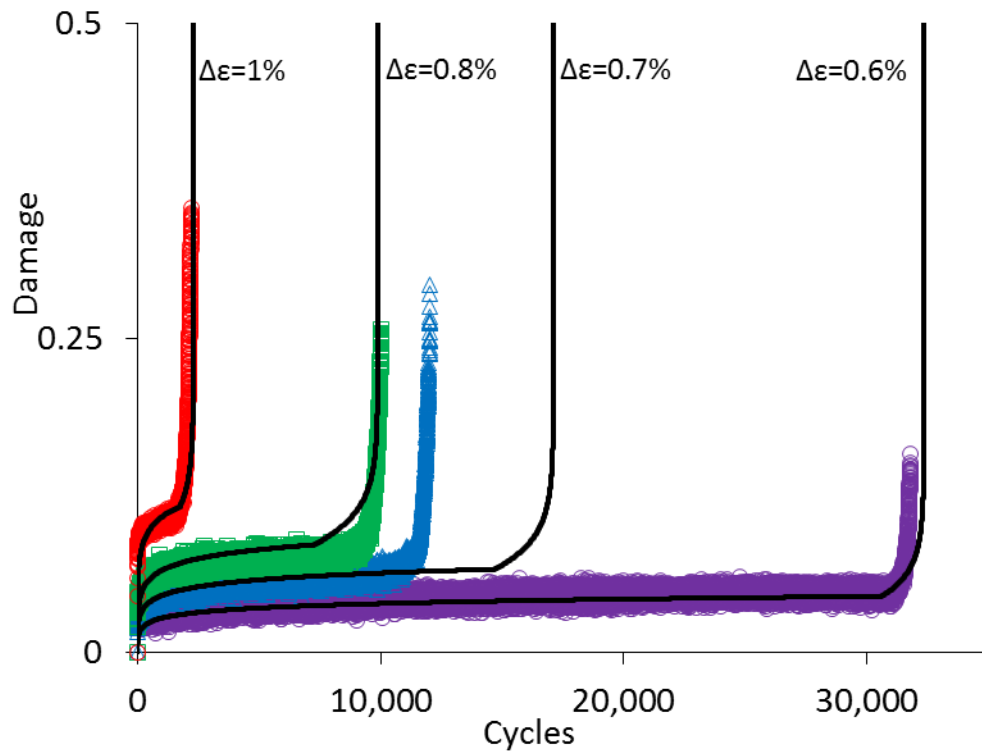


Figure 13. The fit achieved between the experimentally observed damage and the damage evolution predicted using the two-stage LCF model.

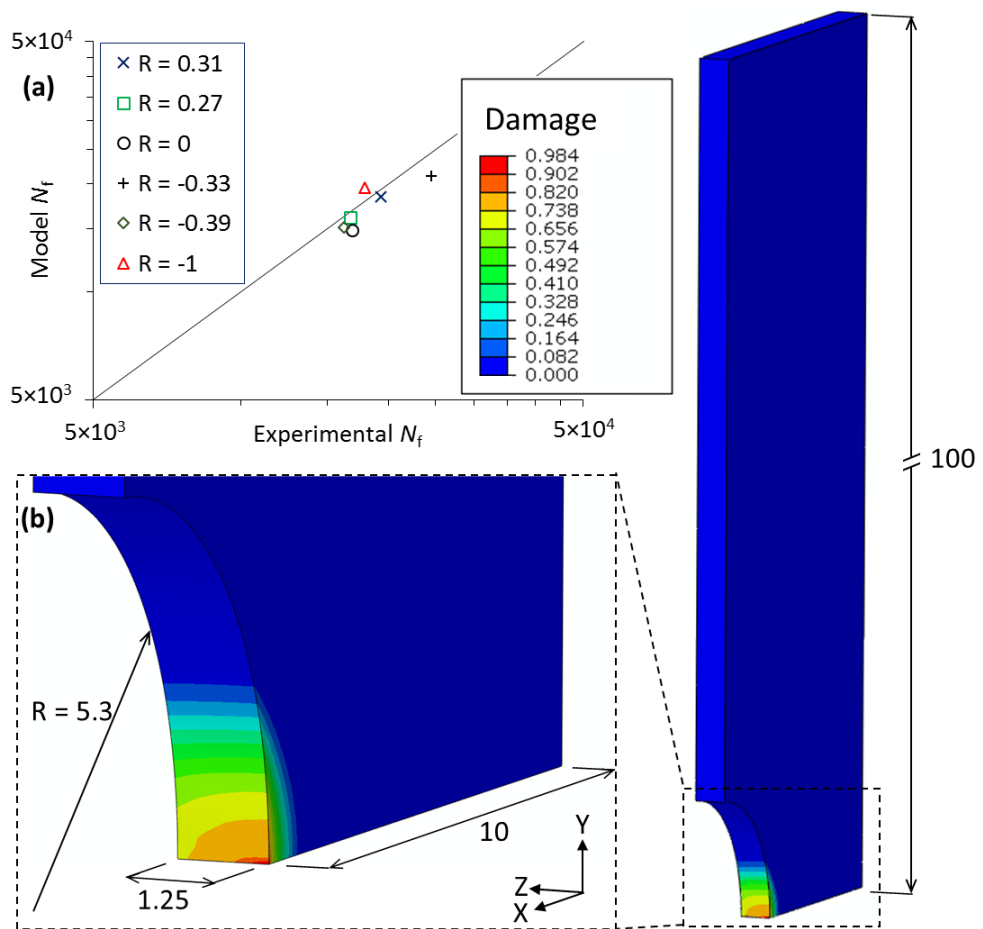


Figure 14. (a) Comparative plot of the experimentally observed and model predicted lives for the notched LC4CS specimen. (b) Contour plot of the damage accumulation near failure for the 0.31 stress ratio test.

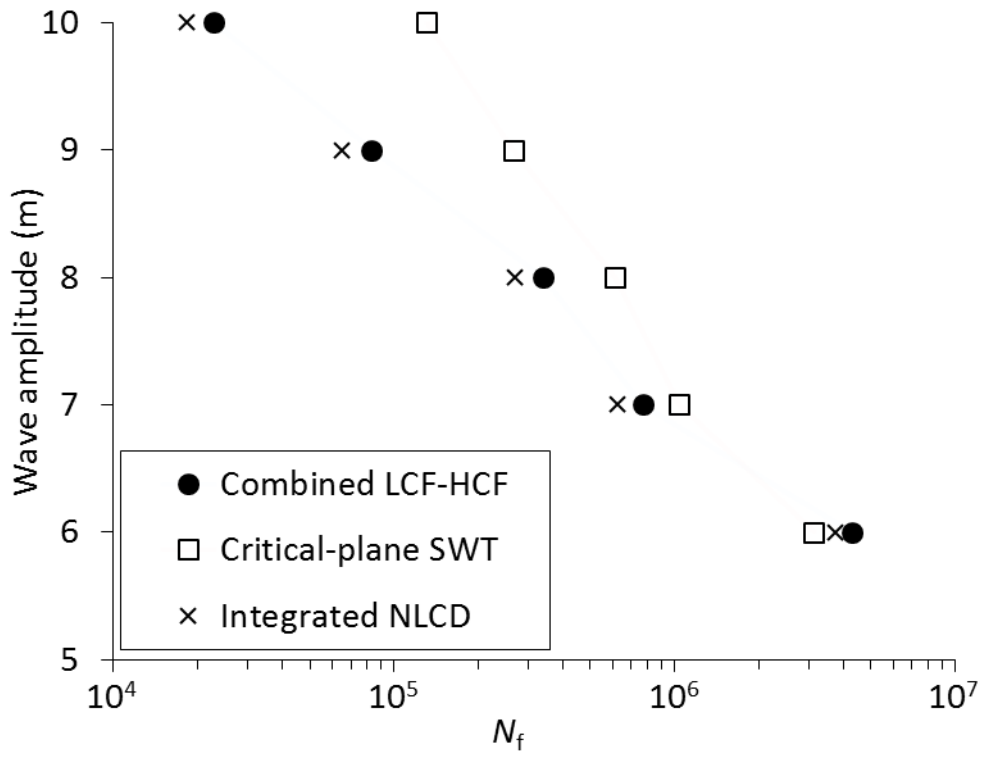


Figure 15. The predicted fatigue lives of the SCR girth obtained using the combined LCF-HCF, critical-plane SWT and integrated NLCD models.

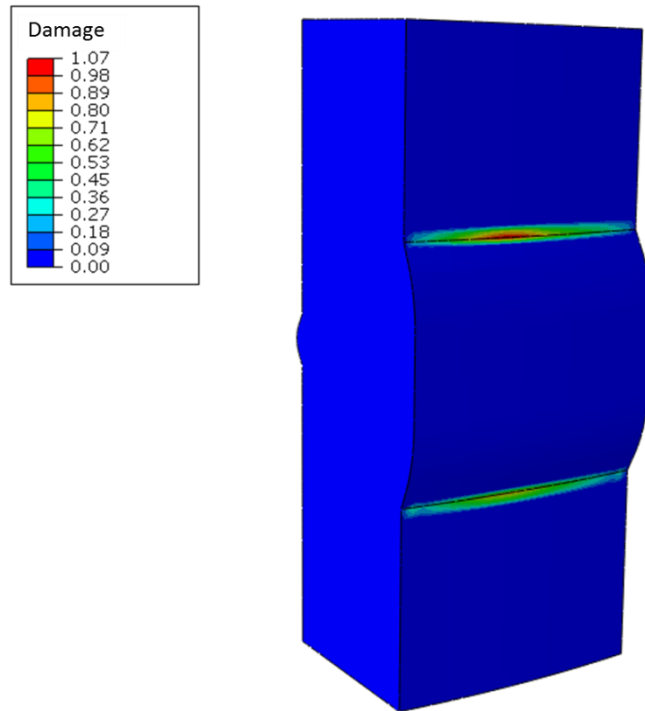


Figure 16. Contour plot of damage accumulation at the X100Q SCR girth weld at failure for the 7 m wave amplitude case. The failure location is at the extreme fibre from the resultant bending moment at the weld toe.

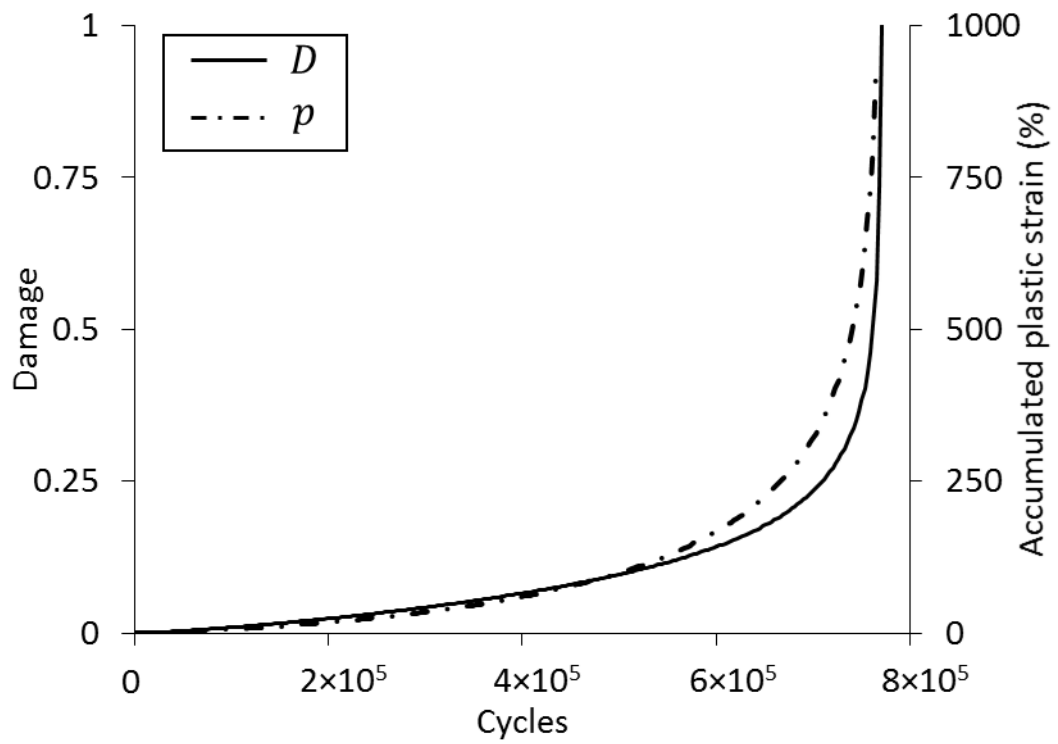


Figure 17. The evolution of damage accumulation and accumulated plastic strain at the failure location of the SCR girth weld (shown in Figure 16) for the 7 m wave amplitude case.